

Article

Hydrogen Production from Methanol Steam Reforming over TiO₂ and CeO₂ Pillared Clay Supported Au Catalysts

Rongbin Zhang ¹, Chuanqing Huang ¹, Lijuan Zong ¹, Kun Lu ¹, Xuewen Wang ¹
and Jianxin Cai ^{2,*}

¹ Department of Chemistry, Institute of Applied Chemistry, Nanchang University, No. 999 Xuefu Road, Nanchang 330031, China; rbzhang@ncu.edu.cn (R.Z.); cqhuang@email.ncu.edu.cn (C.H.); 407028714047@email.ncu.edu.cn (L.Z.); kunlu@email.ncu.edu.cn (K.L.); wangxuewen@ncu.edu.cn (X.W.)

² School of Resources Environmental & Chemical Engineering, Nanchang University, No. 999 Xuefu Road, Nanchang 330031, China

* Correspondence: cjx@ncu.edu.cn

Received: 22 December 2017; Accepted: 22 January 2018; Published: 25 January 2018

Abstract: Methanol steam reforming is a promising process for the generation of hydrogen. In this study, Au catalysts supported on modified montmorillonite were prepared and their catalytic activity for methanol steam reforming was investigated at 250–500 °C. The physical and chemical properties of the as-prepared catalysts were characterized by Brunauer–Emmet–Teller method (BET), X-ray diffraction (XRD), transmission electron microscopic (TEM), scanning electron microscopy (SEM), X-ray photoelectron spectroscopy (XPS), Inductively Coupled Plasma (ICP), and thermogravimetric analysis (TGA). For the catalysts examined, Au-Ti-Ce/Na-ABen exhibits the best catalytic performance with methanol conversion of 72% and H₂ selectivity of 99% at 350 °C. This could be attributed to Au, Ce, and Ti species which form a solid solution and move into the interlayer space of the bentonite leading to a high surface area, large average pore volume, large average pore diameter, and small Au particle size. We considered that the synergistic effect of the crosslinking agent, the Ce species, and the Au active sites were responsible for the high activity of Au-Ti-Ce/Na-ABen catalyst for methanol steam reforming.

Keywords: Au catalysts; steam reforming of methanol; cross-linking agent; ceria; synergistic effect

1. Introduction

Hydrogen is considered one of the best energy carriers to satisfy the ever-growing demand for a clean and sustainable energy supply with the continuous reduction of fossil fuels [1–3]. However, the controlled storage and release of hydrogen is still a critical, challenging, and urgently required issue for fuel cell based hydrogen economy [4–6]. Recently among hydrogen-storage materials for mobile applications, methanol, which is readily available and considered as a sustainable energy carrier since it can be produced from renewable sources, has been recognized as a good feedstuff for high-purified hydrogen production due to its high hydrogen/carbon ratio and safe handling [7–11]. Moreover [3,4], methanol has no C-C bonds, and can be reformed at a relatively low temperature (200–300 °C) with low risk of coke formation. Although methanol is highly toxic and miscible in water, it has the advantage of being biodegradable, liquid at atmospheric conditions, and has a high hydrogen to carbon ratio [12]. During the reaction, this range of temperatures is very low when compared to other common fuels such as methane, which is reformed above 500 °C, and ethanol with a reforming temperature around 400 °C [13,14]. Therefore, methanol is considered as one of the most promising sources for hydrogen production via the steam reforming of methanol (SRM): $\text{CH}_3\text{OH} + \text{H}_2\text{O} \rightleftharpoons \text{CO}_2 + 3\text{H}_2$, $\Delta H^\circ = 49.5 \text{ kJ}\cdot\text{mol}^{-1}$ [15–17].

Recently, a lot of metal catalyst systems, which are divided into two main groups—copper-based and groups 8–10 metal-based catalysts—were tested for hydrogen generation from the steam reforming of methanol [11,18]. Although copper-based catalysts are the most commonly used for the methanol steam reforming reaction (MSR) due to their high activity and selectivity, it is well known that these catalysts can be deactivated by thermal sintering. Thus, it is required to search for other types of catalysts [19–23]. In comparison to Cu-based, group 8–10 catalysts are highly stable and possess similar selectivity. However, the catalytic activity of the latter catalysts has the disadvantage of producing less hydrogen than the copper-based ones [18,24–26].

Montmorillonite is the most popular type of clay applied in pillaring processes and at the same time has attracted worldwide attention recently as a particular fascinating material [26]. Clays are low-cost, abundant natural materials and present many advantages, e.g., recyclability, large surface areas and high exchange capacities. Many industrial processes use clay-based catalysts [27]. Natural bentonite (Ben) is a calcium montmorillonite. Compared with Ca-bentonite, Na-bentonite has higher cation exchange capacity, slower adsorption rate, and larger expansion potential. In addition, the colloids of Na-bentonite show better dispersion and thermal stability [28,29]. One of the methods for preparing this kind of material is to prepare the metal nanoparticles supported on an inorganic pillared clay [30,31]. The cationic layered clays can be transformed into highly porous structures by exchanging interlayer charge compensating cations with large inorganic polymeric oxy-hydroxy cationic species [32–34]. Deposition of such pillars into the interlayer space resulted in a significant increase of the surface area and microporosity of the clay materials [35]. The hydroxyl polycations of polynuclear metals, such as Al, Zr, Ti, Cr, and Fe, are types of inorganic pillaring agents currently being widely studied [36,37]. The TiO₂-pillared clays have large pore sizes allowing further incorporation of active ingredients without hindering pore diffusion and have high thermal and hydrothermal stability, and also show good catalytic performances [38]. As a kind of clay, bentonite has been widely used in many industries as filter material, adsorbent etc. [39]. Bentonite used as catalyst support is an important research area, drawing much attention due to its large surface area and moderate reactivity [40–49].

Cerium oxide supported Au catalysts have been studied in recent years [50–53], and it has been found that CeO₂ promotes activity of Au catalysts [54–56]. The aim of this work was to use the interlayer space of modified bentonite to enclose Au nanoparticles by the Ti cross-linking method. By means of various characterization techniques, the physical and chemical properties of supports and Au catalysts were analyzed and studied, and the catalytic performance in the steam reforming of methanol was evaluated in a fix-bed micro-reactor

2. Experimental

2.1. Materials

Natural bentonite was purchased from Jiangxi Yushan (China). Sodium hydroxide, sodium chloride, hydrochloric acid, chloroauric acid, isopropanol, butyl titanate, and cerium nitrate hexahydrate were obtained from Sinopharm Chemical Reagent Co., Ltd., Shanghai, China. All chemicals were used without further purification.

2.2. Catalyst Preparation

All as-prepared catalyst modified cross-linking agents were prepared by the deposition–precipitation method. Typically natural bentonite (10 g) was pre-treated with H₂SO₄ (50 mL, 20 wt %) and of refluxed for 6 h at 70 °C. Bentonite (Ben) was obtained after centrifuging, washing and drying at 70 °C. Na-bentonite (Na-Ben) was prepared from a mixture of Ben and sodium chloride with a mass ratio of 1:6. After 3 h of stirring at 70 °C, the mixture were centrifuged, washed, and dried at 70 °C overnight. Na-Ben (5 g) was dissolved in HCl (25 mL, 15 wt %) solution at 70 °C for 6 h, washed to pH = 7 with deionized water and dried at 80 °C for 12 h to ready acid-activated Na-Ben. A certain amount of acid-activated Na-Ben was

added to the deionized water and made into a slurry, adjusting to pH = 8 with 0.1 M NaOH. The resulting mixture was stirred at room temperature for 1 h. Then, the alkali-activated Na-Ben (Na-ABen) was obtained by centrifuging, washing and drying at 70 °C for 12 h. Then 10.5 mL of butyl titanate was added to isopropanol (9.8 mL) and stirred until the solution became light yellow, followed by adding 40 mL of distilled water under vigorous stirring until the solution became a white slurry. The above mentioned slurry was sequentially added to concentrated HCl (1 mL) and dried at 50 °C for 12 h to form Ti cross-linking agent. A mixture of Ce(NO₃)₃·6H₂O and Ti cross-linking agent with a molar ratio of Ti/Ce = 10 was added to 4 mL of 0.1 M HAuCl₄ solution at 80 °C and stirred for 24 h. The mixture was mixed with Na-ABen (with a Ti-Ce/Na-ABen ratio of 20 mmol/g). The pH was adjusted to 8 with 1 M NaOH, and the mixture was stirred at 80 °C for 24 h. The suspension was then filtered and the precipitate was washed thoroughly with deionized water to remove the Cl⁻. Finally the catalyst (Au-Ti-Ce/Na-ABen) was dried at 80 °C for 12 h, calcined in air at 400 °C for 3 h. Au/Na-ABen and Au-Ti/Na-ABen were synthesized by the same procedure without addition of Ce(NO₃)₃·6H₂O, Ti cross-linking agent and Ce(NO₃)₃·6H₂O, respectively. For comparison, the Ti cross-linking agent was slowly added into Na-ABen suspension (Ti/Na-ABen = 20 mmol/g) and under vigorous stirring for 3 h. The obtained solid product sample was then centrifuged, washed with deionized water to remove the Cl⁻ and dried at 70 °C for 12 h. Finally, the Ti-Na-ABen was obtained after it was calcined in air at 400 °C for 3 h. Then, the 10 mL 0.1 M HAuCl₄ solution and the above-mention Ti-Na-ABen were adjusted to pH = 8 with 1 M NaOH and the mixture was stirred at 80 °C for 24 h. Finally, the catalyst (Au/Ti-Na-ABen) was dried at 70 °C for 12 h, calcined in air at 400 °C for 3 h. Au/TiO₂ was prepared using a similar procedure without adding Na-ABen. The contents of Au for all samples were kept constant (1.4 wt %).

2.3. Catalyst Characterization

Powder X-ray diffraction (XRD) patterns were recorded on a Bruker AXS D8 Focus diffractometer instrument (Beijing Persee Instrument Co., Ltd., Beijing, China) operating at 40 kV and 40 mA with Cu target K α -ray ($\lambda = 0.154056$ nm) irradiation. Diffraction data (2θ) was collected between 2° and 80° with a scanning rate of 2°/min. For calculation of the interlayer space of ABen by the Bragg equation we used $2d\sin\theta = n\lambda$, where $\lambda = 0.154$ nm is the X-ray wavelength, θ is the Bragg diffraction angle, and n is the series of diffraction [57].

The Brunauer–Emmet–Teller method (BET) were performed at 77 K on Micromeritics ASAP2020 equipment (Micromeritics Instrument (Shanghai) Ltd., Shanghai, China). The samples were degassed in vacuum (≈ 1 μ m Hg) at 200 °C for 300 min. The specific surface area was calculated using the BET model and the pore size distribution was obtained from the adsorption branch of the N₂ isotherm by the Barret-Joyner-Halenda (BJH) model.

Transmission and high resolution transmission electron microscopic (TEM) images were obtained on a JEOL JSM-2010 electron microscope (Japan Electronics Co., Ltd., Tokyo, Japan). The powders were suspended in ethanol for 10 min under ultrasonic treatment before they were deposited onto the carbon-film-coated copper grids. The average gold particle diameter and its distribution were determined by counting at least 50 particles.

Inductively Coupled Plasma-Atomic Emission Spectrometry (ICP-AES) (optima 5300DV, Perkin-Elmer, PE, Waltham, MA, USA) quantitative analyses (Au line 267.595 Å, plasma power 1200W, plasma flow 1.5 L/min).

X-ray photoelectron spectra (XPS) were carried out on a PerkinElmer PHI1600 system (Thermo Fisher Scientific, Waltham, MA, USA) using a single Mg-K-X-ray source operating at 300 W and 15 kV. The spectra were obtained at ambient temperature with an ultrahigh vacuum. The binding energies were calibrated using the C 1s peak of graphite at 284.5 eV as a reference.

The morphologies of the samples were investigated by scanning electron microscopy (SEM, FEI Quanta 200 F, American FEI Company, Hillsboro, Missouri, MO, USA).

Thermogravimetric analysis (TGA) and differential scanning calorimetry (DSC) were simultaneously performed on a CTR-4P instrument (Shanghai precision & scientific instrument Co., Ltd., Shanghai, China) at a linear heating rate of 10 °C/min in air atmosphere.

2.4. Catalytic Activity Measurements

The SRM reaction was carried out in a fix-bed micro-reactor (stainless steel U-shaped tubular reactor, 4 mm i.d.) at atmospheric pressure. The reaction temperature was raised from 250 to 500 °C, and the products were analyzed per 50 °C. Prior to characterization and reaction, the catalyst (100 mg) was reduced in-situ under hydrogen flow (30 mL·min⁻¹) at 150 °C for 2 h, since the main active content of the samples is gold. After catalyst activation, the CH₃OH:H₂O molar ratio was fixed constantly at 1:1. The mixture was injected continuously to a vaporizer by a liquid syringe pump at a rate of 0.175 mL·h⁻¹. Because the methanol reforming produces both liquid and gas phase products, two columns were used for the analysis of the liquid and gas products. The effluent gas stream was analyzed on-line by gas chromatography-thermal conductivity detector (GC-TCD, Shanghai precision & scientific instrument Co., Ltd., Shanghai, China) with a column of TCX-01, with Ar as the carrier gas. The condensate was analyzed by gas chromatography-flame ionization detector (GC-FID, Shanghai precision & scientific instrument Co., Ltd., Shanghai, China) with a column of Porapak-Q, with nitrogen as the carrier gas. At each experimental temperature, the reaction ran for 30 min until the steady state, which was verified by a relative percentage different of less than 5% for two successive runs of effluent gas analysis was achieved. The experimental data were displayed in terms of CH₃OH conversion (%) and H₂ selectivity (%).

$$C_{\text{CH}_3\text{OH}}/\% = \left[1 - \frac{n(\text{C}_{\text{CH}_3\text{OH}})}{n(\text{C}_{\text{CH}_3\text{OH}})_0}\right] \times 100$$

$$S_{\text{H}_2}/\% = \frac{n(\text{H}_2)}{[n(\text{C}_{\text{CH}_3\text{OH}})_0 - n(\text{C}_{\text{CH}_3\text{OH}})] \times 3} \times 100$$

$C_{\text{CH}_3\text{OH}}$ and S_{H_2} present the conversion of CH₃OH and the selectivity of H₂, respectively. $n(\text{CH}_3\text{OH})$, $n(\text{H}_2)$, and $n(\text{CH}_3\text{OH})_0$ present the mole contents of methanol and H₂ of the outlet and the mole content of methanol in the feed, respectively.

3. Results and Discussion

3.1. Characterization

To detect the surface properties of the as-prepared catalysts, X-ray photoelectron spectroscopy (XPS) was employed to examine the content and types of Au species. The results of Au contents of all prepared samples were simultaneously measured by ICP, as shown in Table 1 (and Figure S1 in Supporting Information). It can be seen that Au exists in the form of Au⁰ and Au^{x+} oxidation states with the relative intensities of Au⁰ and Au^{x+} being 41% and 59% respectively. Probably because the reduction at 150 °C is not so strong to reduce all the gold in the oxidized states, the gold is present also as Au^{x+} in a larger amount. We found that this value of actual gold content examined by ICP is much higher than the surface gold content examined by XPS. It indicates that most of the Au nanoparticles moved into the interlayers of the clay. The actual gold contents of the Au-Ti/Na-ABen and Au-Ti-Ce/Na-ABen catalysts are much higher than that of Au/Ti-Na-ABen. This could be attributed to the surface gold content of Au/Ti-Na-ABen being higher than Au-Ti/Na-ABen and Au-Ti-Ce/Na-ABen. The results show that the Ti cross-linking compound could result in the gold moving into the interlayer space of bentonite and improving the actual gold content of the sample.

Table 1. The Au contents of the prepared samples measured by Inductively Coupled Plasma (ICP), X-ray photoelectron spectroscopy (XPS), D_{Au} and TOF_{CH_3OH} .

| Sample | Au (%) | | D_{Au} ^a (%) | TOF_{CH_3OH} ^b (s^{-1}) |
|------------------|--------|-------|---------------------------|--|
| | ICP | XPS | | |
| Au/Na-ABen | 0.51 | 0.054 | 8.3 | 0.05 |
| Au/Ti-Na-ABen | 0.54 | 0.116 | 10.0 | 0.32 |
| Au-Ti/Na-ABen | 1.30 | 0.094 | 12.5 | 0.33 |
| Au-Ti-Ce/Na-ABen | 1.34 | 0.086 | 16.7 | 0.41 |

^a The Au dispersion values of the surface of prepared catalysts (D_{Au}) was calculated by $D_{Au} = 1/Diameter_{Au}$, in which the d stands for the mean diameter of prepared catalysts from TEM. ^b The TOF_{CH_3OH} values of prepared catalysts were calculated according to the original data provided by a temperature of 673 K and as conversion of methanol by the composite catalysts per second and the number of surface Au atoms determined by XPS [58].

Figure 1 shows the powder X-ray diffraction pattern of the catalyst. XRD was used to determine the crystalline phases of catalyst. The 2θ angles at about 19.88° and 26.78° belong to kaolinite and SiO_2 , respectively. The peak at 38.2° show that Au phase formed in the Au-Ti/Na-ABen and Au-Ti-Ce/Na-ABen catalysts, since the catalyst produced by compound cross-linking can improve the load of gold, while no Au reflection peak was observed for the Au/Ti-Na-ABen catalyst. This is because the gold in the Au/Ti-Na-ABen catalyst was highly dispersed fine nano-particles on the surface [59], and the actual Au content in this sample was not high. The reflection peak of CeO_2 was not observed since CeO_2 was highly dispersed in the interlayer space of bentonite. The broad peaks of the TiO_2 phase are found in the Au-Ti-Ce/Na-ABen catalyst. The probable reason is that a solid solution may be formed due to the Ce^{4+} species in the TiO_2 lattice.

Table 2 shows the 2θ and $d(001)$ spacing of the prepared samples. It shows that the original $d(001)$ spacing of Ca-bentonite is 12.73 Å. After the Na ion exchange and activation process, the $d(001)$ spacing of Na-ABen became 14.91 Å. While, the introduction of Au to the Na-ABen resulted in the reduction of the $d(001)$ spacing of Au/Na-ABen to 12.08 Å, while, the cross-linking agent could obviously increase the $d(001)$ spacing of the bentonite. Ti-Na-ABen, Au/Ti-Na-ABen, Au-Ti/Na-ABen, and Au-Ti-Ce/Na-ABen show $d(001)$ spacings of 15.12, 15.27, 15.82, and 16.30 Å, respectively. The shifting of the 2θ value from 5.840° to 5.410° , clearly demonstrates the expansion of the interlayers of bentonite during the pillaring process.

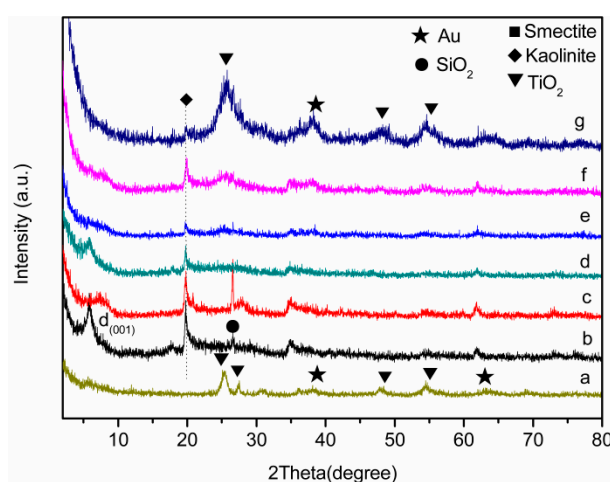
**Figure 1.** X-ray diffraction (XRD) patterns of the samples: (a) Au/ TiO_2 ; (b) Na-ABen; (c) Au/Na-ABen; (d) Ti-Na-ABen; (e) Au/Ti-Na-ABen; (f) Au-Ti/Na-ABen; (g) Au-Ti-Ce/Na-ABen.

Table 2. The 2 θ and d(001) spacing of the samples.

| Sample | 2 θ | d (Å) |
|------------------|------------|-------|
| Ben | 6.930 | 12.73 |
| Na-ABen | 5.924 | 14.91 |
| Au/Na-ABen | 7.313 | 12.08 |
| Ti-Na-ABen | 5.840 | 15.12 |
| Au/Ti-Na-ABen | 5.783 | 15.27 |
| Au-Ti/Na-ABen | 5.581 | 15.82 |
| Au-Ti-Ce/Na-ABen | 5.410 | 16.30 |

The BET surface area, average pore volume, and average pore diameter for all prepared samples are shown in Table 3. The surface area of Ben increased from 35.5 to 134.3 m²/g after Na ion exchange and the activation process. This is because the inorganic salt and metal oxide in the interlayer of bentonite were removed, which makes the pores of the clay dredged. The cross-linking agent pillared catalysts show an even higher surface area, since the components of crosslinking went into the interlayer of bentonite and forced the layers of clay apart [60]. However, the surface area of Na-ABen and Ti-Na-ABen decreased from 134.3 and 210.6 m²/g to 112.9 and 191.8 m²/g, respectively, after the loading of Au (Au/Na-ABen and Au/Ti-Na-ABen) This could be mainly ascribed to the Au nanoparticles going into the pores of the support, which did not function as a pillar, and blocked some of the pores. The surface areas of Au-Ti/Na-ABen and Au-Ti-Ce/Na-ABen are higher than those of Au/Na-ABen and Au/Ti-Na-ABen, since Au together with Ce and Ti cross-linking agent move into the interlayer of bentonite and lead to the increased layer spacing of bentonite. It was observed that the Au-Ti-Ce/Na-ABen catalyst has a larger surface area than Au-Ti/Na-ABen, this may be due to Ce⁴⁺ and part of the Au species migrating into the interlayers by the synergistic effect. These results agreed well with those found by XRD measurement (Table 2).

Table 3. Brunauer–Emmet–Teller (BET) surface area, pore volume, and average pore size of the samples.

| Sample | Average Pore Diameter (nm) | Pore Volume (cm ³ /g) | S _{BET} (m ² /g) |
|---------------------|----------------------------|----------------------------------|--------------------------------------|
| Au/TiO ₂ | 7.95 | 0.123 | 62.0 |
| Ben | 6.68 | 0.059 | 35.5 |
| Na-ABen | 4.64 | 0.156 | 134.3 |
| Au/Na-ABen | 5.60 | 0.158 | 112.9 |
| Ti-Na-ABen | 5.48 | 0.289 | 210.6 |
| Au/Ti-Na-ABen | 5.90 | 0.283 | 191.8 |
| Au-Ti/Na-ABen | 9.91 | 0.621 | 250.7 |
| Au-Ti-Ce/Na-ABen | 9.64 | 0.677 | 281.0 |

SEM images of Au/Na-ABen, Au/Ti-Na-ABen, Au-Ti/Na-ABen, and Au-Ti-Ce/Na-ABen catalysts are illustrated in Figure 2. It was found that the particles size was not uniform, and there were some large particles in the sample. This could be mainly attributable to the crosslinking agent precursors of organic volatiles moving out quickly during the calcination so that its frame has no time to contract evenly. In addition, some irregular frameworks emerged on the surface of bentonite due to the pillared content increases.

The morphologies of the supported Au catalysts are characterized by typical transmission electron microscopy (TEM). It is observed clearly from Figures 3a–c and 4d that both Au particles, Au-Ti pillaring species, and Au-Ti-Ce pillaring species appear as nanoparticles, and the mean diameters of them are about 12, 10, 8, and 6 nm, respectively. Au/Ti-ABen catalyst had the largest Au particle size, Furthermore, for the Au/Ti-ABen catalyst, Au particles dispersed unevenly and reunion. For the Au-Ti/ABen and Au-Ti-Ce/ABen catalysts, the pillaring species evenly dispersed on the surface of the bentonite and part of the pillaring species were dispersed to enter interlayers. Compared with other catalysts, Au/Na-ABen catalyst which had the largest Au particle size bring about the lower catalytic activity. For the Au-Ti/Na-ABen and Au-Ti-Ce/Na-ABen catalysts with special, pillaring species

evenly dispersed on the surface of bentonite, parts of the pillaring species entered into the interlayer space of the bentonite. Furthermore, all the mean diameter values are much smaller than the clay interlayer spacing. These results provide further support to confirm that the species of Au nanoparticles can be inserted into the clay interlayer to improve the catalyst for methanol steam reforming.

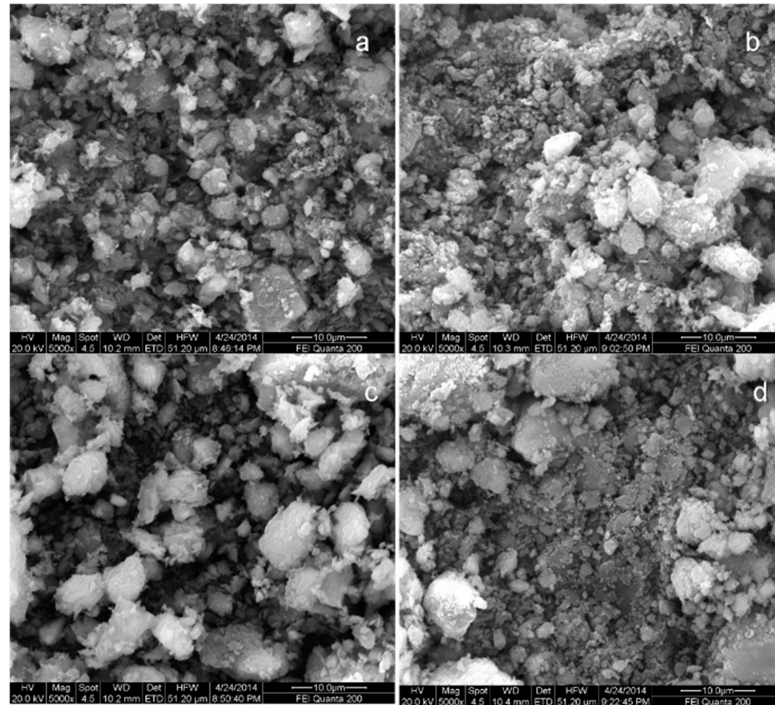


Figure 2. Scanning electron microscopy (SEM) images of the catalysts: (a) Au/Na-ABen; (b) Au/Ti-Na-ABen; (c) Au-Ti/Na-ABen; (d) Au-Ti-Ce/Na-ABen.

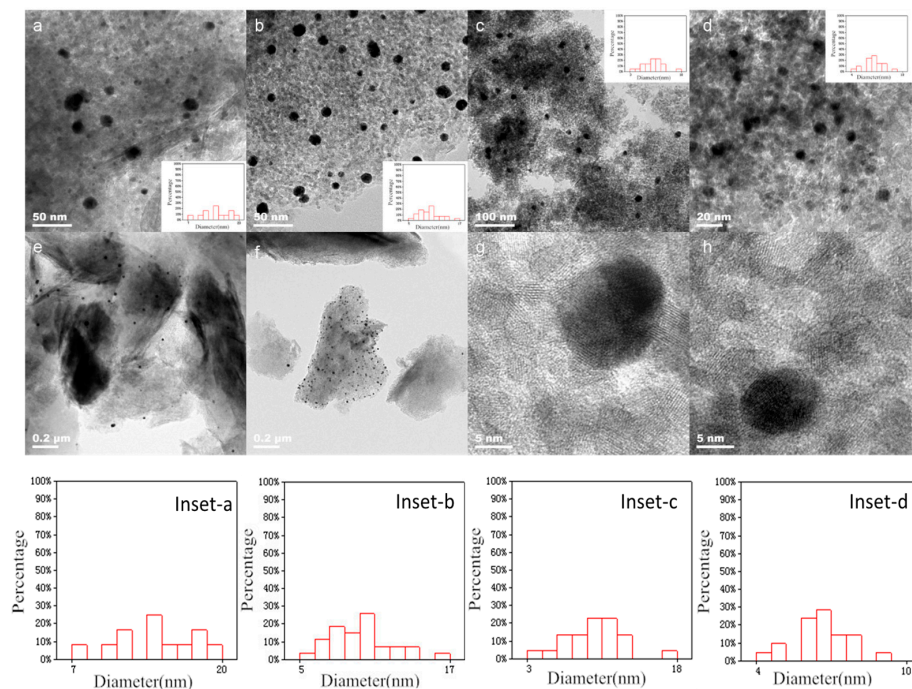


Figure 3. Transmission electron microscopic (TEM) images of the samples. (a,e) Au/Na-ABen; (b,f) Au/Ti-Na-ABen; (c,g) Au-Ti/Na-ABen; (d,h) Au-Ti-Ce/Na-ABen.

The thermal stability of the catalyst is very important for practical application. Thus it is necessary that the thermal stability of the as-prepared catalysts are also evaluated by thermogravimetric analysis (TGA). Figure 4 show the TGA curves of ABen, Au/Na-ABen, Au-Ti/ABen and Au/Ti-Na-ABen nanocomposite under an air atmosphere. The weight of ABen gradually decreased as the temperature was increased to 200 °C and the TGA profile of the others indicated that a significant weight loss was then observed at temperature ranging from 30 to 100 °C. This could be mainly assigned to the removal of adsorbed water molecules. There was not a significant weight loss obvious as the temperature was increased to 800 °C for the TGA curves of the as-prepared catalysts. The results indicate that the as-prepared catalysts modified by the cross-linking agent possess more a better thermal stability than the catalysts without modification by cross-linking agent.

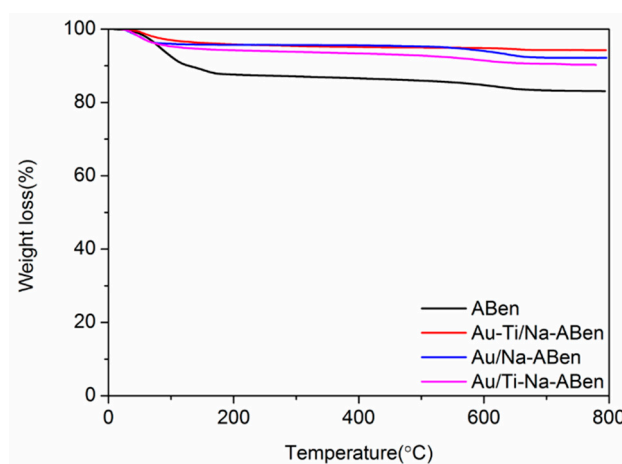


Figure 4. Thermogravimetric analysis (TGA) curves of ABen, Au-Ti/Na-ABen, Au/Na-ABen, and Au/Ti-Na-ABen in an air atmosphere.

3.2. Catalytic Activity Tests

The catalytic performances of the Au/TiO₂, Au/Na-ABen, Au/Ti-Na-ABen, Au-Ti/Na-ABen and Au-Ti-Ce/Na-ABen catalysts for the SRM reaction were evaluated at 250–500 °C and the results are shown in Figure 5. As shown in Figure 5a, the activity of Au/TiO₂ and Au/Na-ABen is much lower than Au/Ti-Na-ABen, Au-Ti/Na-ABen, and Au-Ti-Ce/Na-ABen, since the BET surface areas and particle size of the Au/TiO₂ and Au/Na-ABen are much smaller than the other samples. In addition, the methanol conversion increases as the temperature rises for Au/Ti-Na-ABen, Au-Ti/Na-ABen, and Au-Ti-Ce/Na-ABen. For Au/TiO₂ and Au/Na-ABen, the methanol conversion increases as the temperature rises at the beginning, and then decreases as the temperature becomes higher. It might be attributed to the Au particles on the Au/TiO₂ and Au/Na-ABen aggregate becoming less active. Since Au-Ti compound as cross-linking agent for Au-Ti/Na-ABen could make the Au nanoparticles move into the interlayer of bentonite clay and be confined in the interspace, the Au-Ti/Na-ABen catalysts show better catalytic activity than Au/Ti-Na-ABen. Au-Ti-Ce/Na-ABen shows the best activity for the SRM reaction and reaches more than 80% methanol conversion at 400 °C. This could be attributed to the Au-Ti-Ce which can also move into the interlayer space of bentonite and enlarge the d(001) spacing of bentonite. In addition, the Au-Ti-Ce cross-linking agent results in a smaller Au particle for the Au-Ti-Ce/Na-ABen sample, and more Au is defined in the interlayer space of bentonite. It is clear that the cerium obviously promoted the activity of methanol conversion.

Figure 5b shows that the H₂ selectivity is higher than 95% at 250–350 °C for all catalysts except Au/TiO₂. The H₂ selectivity decreased as the temperature became higher than 350 °C for most of the catalysts. This is because the water-gas shift reaction is endothermic. Thus, as the temperature rises, the reaction balance moves and favors the production of CO, and the H₂ selectivity decreases [61]. It should be mentioned that the catalytic performance of the Au-Ti-Ce/Na-ABen catalyst is the best in

the present work. However, its activity as well as selectivity is not as good as the reported Cu-Al spinel catalysts, which have been commercialized for industrial methanol reforming [62,63]. Following the reviewer's suggestions, we also tested the stability and selectivity of the samples at 400 °C for 120 h (Figure 5c). It was found that all samples show excellent stability without obvious deactivation. The CO and CO₂ selectivities at 400 °C over Au-Ti-Ce/Na-ABen are 0.2% and 99.7%, respectively. In terms of TOF_{CH₃OH} by counting the surface number of Au atoms in the catalysts (Table 1), it can be seen that the TOF of Au-Ti-Ce/Na-ABen (0.41 s⁻¹) is the highest one among those of all catalysts. This indicates that the addition of cerium can remarkably improve the TOF value of the Au-Ti/Na-ABen catalyst.

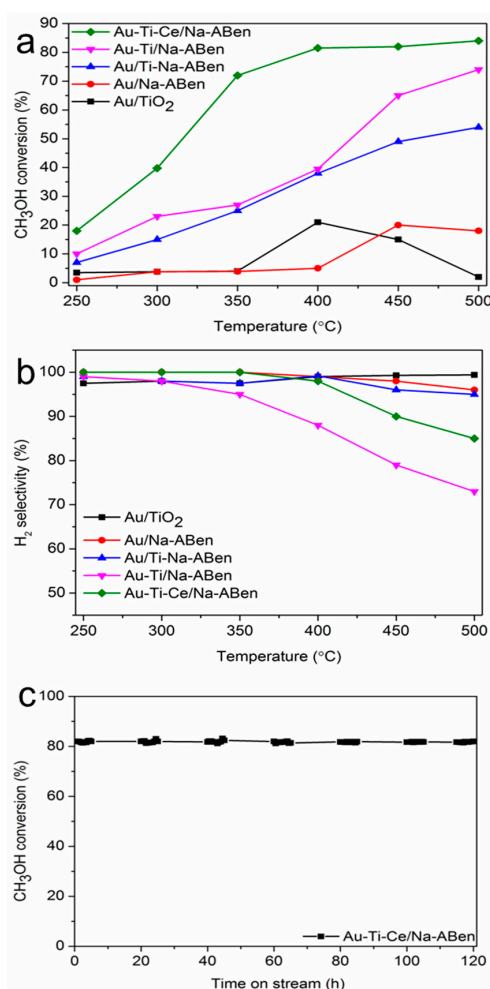


Figure 5. The catalytic performances of the prepared samples for the SRM reaction. (a) Methanol conversion; (b) H₂ selectivity; (c) stability.

4. Conclusions

The modification of the layer clays and pillared clay-based catalysts by a cross-linking agent apparently enhanced the thermal stability of the catalyst and enlarged the interlayer spacing between the two bentonite layers. The Au-Ti-Ce/Na-ABen catalyst shows the best activity and best H₂ selectivity of all the samples. As evidenced by XRD, ICP, and XPS characterizations, the Au, Ce, and Ti species could form a solid solution and move into the interlayer space of the bentonite in the case of Au-Ti-Ce/Na-ABen. Thus it is apparent that the synergistic effect of the crosslinking agent, Ce species, and Au active sites are responsible for the high activity of the Au-Ti-Ce/Na-ABen catalyst for methanol steam reforming.

Supplementary Materials: The following are available online at www.mdpi.com/2076-3417/8/2/0176/s1, Figure S1: The XPS Au(4f) of Au-Ti-Ce/Na-ABen.

Acknowledgments: This work was financially supported by the National High Technology Research and Development Program of China (2015AA03A401 supported by National Natural Science Foundation of China (Grant No. 21263016, 21363015 and 21365013).

Author Contributions: Rongbin Zhang and Chuangqing Wang conceived and designed the experiments; Lijuan Zong and Kun Lu performed the experiments; Kun Lun and Xuewen Wang analyzed the data; Rongbin Zhang and Jianxin Cai wrote the paper; Jianxin Cai proofread the manuscript.

Conflicts of Interest: The authors declare no conflict of interest.

References

1. Momirlan, M.; Veziroglu, T.N. Current status of hydrogen energy. *Renew. Sustain. Energy Rev.* **2002**, *6*, 141–179. [[CrossRef](#)]
2. El-Shahat, A. Hydrogen Fuel Cells Progressing as Power Source. *Nat. Gas Electr.* **2016**, *33*, 7–11. [[CrossRef](#)]
3. Bockris, J.O. Hydrogen. *Materials* **2011**, *4*, 2073–2091. [[CrossRef](#)] [[PubMed](#)]
4. Momirlan, M.; Veziroglu, T.N. The properties of hydrogen as fuel tomorrow in sustainable energy system for a cleaner planet. *Int. J. Hydrog. Energy* **2005**, *30*, 795–802. [[CrossRef](#)]
5. Schlapbach, L.; Zuttel, A. Hydrogen-storage materials for mobile applications. *Nature* **2001**, *414*, 353–358. [[CrossRef](#)] [[PubMed](#)]
6. Edwards, P.P.; Kuznetsov, V.L.; David, W.I.F.; Brandon, N.P. Hydrogen and fuel cells: Towards a sustainable energy future. *Energy Policy* **2008**, *36*, 4356–4362. [[CrossRef](#)]
7. Liu, N.; Yuan, Z.; Wang, S.; Zhang, C.; Wang, S.; Li, D. Characterization and performance of a ZnO–ZnCr₂O₄/CeO₂–ZrO₂ monolithic catalyst for methanol auto-thermal reforming process. *Int. J. Hydrog. Energy* **2008**, *33*, 1643–1651. [[CrossRef](#)]
8. Hamelinck, C.N.; Faaij, A.P.C. Future prospects for production of methanol and hydrogen from biomass. *J. Power Sources* **2002**, *111*, 1–22. [[CrossRef](#)]
9. Agrell, J.; Birgersson, H.; Boutonnet, M.; Melián-Cabrera, I.; Navarro, R.M.; Fierro, J.L.G. Production of hydrogen from methanol over Cu/ZnO catalysts promoted by ZrO₂ and Al₂O₃. *J. Catal.* **2003**, *219*, 389–403. [[CrossRef](#)]
10. Hong, X.; Ren, S. Selective hydrogen production from methanol oxidative steam reforming over Zn–Cr catalysts with or without Cu loading. *Int. J. Hydrog. Energy* **2008**, *33*, 700–708. [[CrossRef](#)]
11. Sá, S.; Silva, H.; Brandão, L.; Sousa, J.M.; Mendes, A. Catalysts for methanol steam reforming—A review. *Appl. Catal. B* **2010**, *99*, 43–57. [[CrossRef](#)]
12. Lwin, Y.; Daud, W.R.W.; Mohamad, A.B.; Yaakob, Z. Hydrogen production from steam–methanol reforming: Thermodynamic analysis. *Int. J. Hydrog. Energy* **2000**, *25*, 47–53. [[CrossRef](#)]
13. Patel, S.; Pant, K.K. Activity and stability enhancement of copper–alumina catalysts using cerium and zinc promoters for the selective production of hydrogen via steam reforming of methanol. *J. Power Sources* **2006**, *159*, 139–143. [[CrossRef](#)]
14. Onsuratoom, S.; Puangpetch, T.; Chavadej, S. Comparative investigation of hydrogen production over Ag-, Ni-, and Cu-loaded mesoporous-assembled TiO₂–ZrO₂ mixed oxide nanocrystal photocatalysts. *Chem. Eng. J.* **2011**, *173*, 667–675. [[CrossRef](#)]
15. Shi, Q.; Liu, C.; Chen, W. Hydrogen production from steam reforming of ethanol over Ni/MgO–CeO₂ catalyst at low temperature. *J. Rare Earths* **2009**, *27*, 948–954. [[CrossRef](#)]
16. Wang, H.; Zhang, L.; Li, M.; Liu, Y.; Bai, X. Co/CeO₂ for ethanol steam reforming: Effect of ceria morphology. *J. Rare Earths* **2013**, *31*, 565–571. [[CrossRef](#)]
17. Zhu, X.; Wang, H.; Wei, Y.; Li, K.; Cheng, X. Hydrogen and syngas production from two-step steam reforming of methane over CeO₂–Fe₂O₃ oxygen carrier. *J. Rare Earths* **2010**, *28*, 907–913. [[CrossRef](#)]
18. Xu, X.; Shuai, K.; Xu, B. Review on Copper and Palladium Based Catalysts for Methanol Steam Reforming to Produce Hydrogen. *Catalysts* **2017**, *7*, 183. [[CrossRef](#)]
19. Papavasiliou, J.; Avgouropoulos, G.; Ioannides, T. Production of hydrogen via combined steam reforming of methanol over CuO–CeO₂ catalysts. *Catal. Commun.* **2004**, *5*, 231–235. [[CrossRef](#)]

20. Choi, H.-J.; Kang, M. Hydrogen production from methanol/water decomposition in a liquid photosystem using the anatase structure of Cu loaded. *Int. J. Hydrog. Energy* **2007**, *32*, 3841–3848. [[CrossRef](#)]
21. Yao, C.-Z.; Wang, L.-C.; Liu, Y.-M.; Wu, G.-S.; Cao, Y.; Dai, W.-L.; He, H.-Y.; Fan, K.-N. Effect of preparation method on the hydrogen production from methanol steam reforming over binary Cu/ZrO₂ catalysts. *Appl. Catal. A* **2006**, *297*, 151–158. [[CrossRef](#)]
22. Jeong, H.; Kim, K.I.; Kim, T.H.; Ko, C.H.; Park, H.C.; Song, I.K. Hydrogen production by steam reforming of methanol in a micro-channel reactor coated with Cu/ZnO/ZrO₂/Al₂O₃ catalyst. *J. Power Sources* **2006**, *159*, 1296–1299. [[CrossRef](#)]
23. Fornari, A.C.; Menechini Neto, R.; Lenzi, G.G.; dos Santos, O.A.A.; de Matos Jorge, L.M. Utilization of sol-gel CuO-ZnO-Al₂O₃ catalysts in the methanol steam reforming for hydrogen production. *Can. J. Chem. Eng.* **2017**, *95*, 2258–2271. [[CrossRef](#)]
24. Patel, N.; Kale, A.; Miotello, A. Improved dehydrogenation of ammonia borane over Co-P-B coating on Ni: A single catalyst for both hydrolysis and thermolysis. *Appl. Catal. B* **2012**, *111–112*, 178–184. [[CrossRef](#)]
25. Suwa, Y.; Ito, S.-I.; Kameoka, S.; Tomishige, K.; Kunimori, K. Comparative study between Zn-Pd/C and Pd/ZnO catalysts for steam reforming of methanol. *Appl. Catal. A* **2004**, *267*, 9–16. [[CrossRef](#)]
26. Ummartyotin, S.; Bunnak, N.; Manuspiya, H. A comprehensive review on modified clay based composite for energy based materials. *Renew. Sustain. Energy Rev.* **2016**, *61*, 466–472. [[CrossRef](#)]
27. Figueras, F. Pillared Clays as Catalysts. *Catal. Rev.* **1988**, *30*, 457–499. [[CrossRef](#)]
28. Karakaya, M.Ç.; Karakaya, N.; Bakır, S. Some properties and potential applications of the Na- and Ca-bentonites of ordu (N.E. Turkey). *Appl. Clay Sci.* **2011**, *54*, 159–165. [[CrossRef](#)]
29. Ding, Z.; Klopogge, J.T.; Frost, R.L.; Lu, G.Q.; Zhu, H.Y. Porous Clays and Pillared Clays-Based Catalysts. Part 2: A Review of the Catalytic and Molecular Sieve Applications. *J. Porous Mater.* **2001**, *8*, 273–293. [[CrossRef](#)]
30. Cool, P.; Vansant, E.F. Pillared Clays: Preparation, Characterization and Applications. In *Synthesis*; Springer: Berlin/Heidelberg, Germany, 1998; pp. 265–288.
31. Klopogge, J.T. Synthesis of Smectites and Porous Pillared Clay Catalysts: A Review. *J. Porous Mater.* **1998**, *5*, 5–41. [[CrossRef](#)]
32. Chmielarz, L.; Piwowska, Z.; Kuśtrowski, P.; Gil, B.; Adamski, A.; Dudek, B.; Michalik, M. Porous clay heterostructures (PCHs) intercalated with silica-titania pillars and modified with transition metals as catalysts for the DeNO_x process. *Appl. Catal. B* **2009**, *91*, 449–459. [[CrossRef](#)]
33. Zhang, Y.; Xu, Y.; Cui, H.; Liu, B.; Gao, X.; Wang, D.; Liang, P. La(III)-loaded bentonite/chitosan beads for defluoridation from aqueous solution. *J. Rare Earths* **2014**, *32*, 458–466. [[CrossRef](#)]
34. Wang, D.; Li, H.; Wang, L.; Zhang, L.; Xu, Y. Effects of chitosan-RE₃₊-bentonite on growth of *Chlorella vulgaris*. *J. Rare Earths* **2010**, *28*, 149–153. [[CrossRef](#)]
35. Chmielarz, L.; Gil, B.; Kuśtrowski, P.; Piwowska, Z.; Dudek, B.; Michalik, M. Montmorillonite-based porous clay heterostructures (PCHs) intercalated with silica-titania pillars—synthesis and characterization. *J. Solid State Chem.* **2009**, *182*, 1094–1104. [[CrossRef](#)]
36. Zhang, H.; Liang, X.; Yang, C.; Niu, C.; Wang, J.; Su, X. Nano γ -Fe₂O₃/bentonite magnetic composites: Synthesis, characterization and application as adsorbents. *J. Alloys Compd.* **2016**, *688*, 1019–1027. [[CrossRef](#)]
37. Vicente, M.A.; Belver, C.; Trujillano, R.; Rives, V.; Álvarez, A.C.; Lambert, J.F.; Korili, S.A.; Gandía, L.M.; Gil, A. Preparation and characterisation of Mn- and Co-supported catalysts derived from Al-pillared clays and Mn- and Co-complexes. *Appl. Catal. A* **2004**, *267*, 47–58. [[CrossRef](#)]
38. Castillo, H.L.D.; Grange, P. Preparation and catalytic activity of titanium pillared montmorillonite. *Appl. Catal. A* **1993**, *103*, 23–34. [[CrossRef](#)]
39. Nafees, M.; Waseem, A. Organoclays as Sorbent Material for Phenolic Compounds: A Review. *Clean Soil Air Water* **2014**, *42*, 1500–1508. [[CrossRef](#)]
40. Yang, H.-C.; Chang, F.-W.; Roselin, L.S. Hydrogen production by partial oxidation of methanol over Au/CuO/ZnO catalysts. *J. Mol. Catal. A Chem.* **2007**, *276*, 184–190. [[CrossRef](#)]
41. Barrer, R.M.; MacLeod, D.M. Activation of montmorillonite by ion exchange and sorption complexes of tetra-alkyl ammonium montmorillonites. *Trans. Faraday Soc.* **1955**, *51*, 1290–1300. [[CrossRef](#)]
42. Tadros, T.F.; Martini, G.; Bahranowski, K.; Serwicka, E.M. Magnetic Resonance in Colloid and Interface Science ESR study of vanadium-doped alumina- and titania-pillared montmorillonites. *Colloids Surf. A Physicochem. Eng. Asp.* **1993**, *72*, 153–160.

43. Phukan, A.; Ganguli, J.N.; Dutta, D.K. ZnCl₂-Zn²⁺-Montmorillonite composite: Efficient solid acid catalyst for benzylation of benzene. *J. Mol. Catal. A Chem.* **2003**, *202*, 279–287. [CrossRef]
44. Feng, J.; Wong, R.S.K.; Hu, X.; Yue, P.L. Discoloration and mineralization of Orange II by using Fe³⁺-doped TiO₂ and bentonite clay-based Fe nanocatalysts. *Catal. Today* **2004**, *98*, 441–446. [CrossRef]
45. Zuo, S.; Zhou, R. Al-pillared clays supported rare earths and palladium catalysts for deep oxidation of low concentration of benzene. *Appl. Surf. Sci.* **2006**, *253*, 2508–2514. [CrossRef]
46. Mo, Z.; Zhang, P.; Zuo, D.; Sun, Y.; Chen, H. Synthesis and characterization of polyaniline nanorods/Ce(OH)₃-Pr₂O₃/montmorillonite composites through reverse micelle template. *Mater. Res. Bull.* **2008**, *43*, 1664–1669. [CrossRef]
47. Chen, C.-C.; Kuo, P.-L. Gold nanoparticles prepared using polyethylenimine adsorbed onto montmorillonite. *J. Colloid Interface Sci.* **2006**, *293*, 101–107. [CrossRef] [PubMed]
48. Razakamanantsoa, A.R.; Barast, G.; Djeran-maigre, I. Hydraulic performance of activated calcium bentonite treated by polyionic charged polymer. *Appl. Clay Sci.* **2012**, *59–60*, 103–114. [CrossRef]
49. Khenifi, A.; Zohra, B.; Kahina, B.; Houari, H.; Zoubir, D. Removal of 2,4-DCP from wastewater by CTAB/bentonite using one-step and two-step methods: A comparative study. *Chem. Eng. J.* **2009**, *146*, 345–354. [CrossRef]
50. Tanaka, A.; Hashimoto, K.; Kominami, H. Preparation of Au/CeO₂ Exhibiting Strong Surface Plasmon Resonance Effective for Selective or Chemoselective Oxidation of Alcohols to Aldehydes or Ketones in Aqueous Suspensions under Irradiation by Green Light. *J. Am. Chem. Soc.* **2012**, *134*, 14526–14533. [CrossRef] [PubMed]
51. Fiorenza, R.; Bellardita, M.; Palmisano, L.; Scirè, S. A comparison between photocatalytic and catalytic oxidation of 2-Propanol over Au/TiO₂-CeO₂ catalysts. *J. Mol. Catal. A Chem.* **2016**, *415*, 56–64. [CrossRef]
52. Zhang, R.; Lu, K.; Zong, L.; Tong, S.; Wang, X.; Feng, G. Gold supported on ceria nanotubes for CO oxidation. *Appl. Surf. Sci.* **2017**, *416*, 183–190. [CrossRef]
53. Freakley, S.J.; He, Q.; Kiely, C.J.; Hutchings, G.J. Gold Catalysis: A Reflection on Where We are Now. *Catal. Lett.* **2014**, *145*, 71–79. [CrossRef]
54. Fiorenza, R.; Bellardita, M.; D'Urso, L.; Compagnini, G.; Palmisano, L.; Scirè, S. Au/TiO₂-CeO₂ Catalysts for Photocatalytic Water Splitting and VOCs Oxidation Reactions. *Catalysts* **2016**, *6*, 121. [CrossRef]
55. Zhang, R.; Lu, K.; Zong, L.; Tong, S.; Wang, X.; Zhou, J.; Lu, Z.-H.; Feng, G. Control synthesis of CeO₂ nanomaterials supported gold for catalytic oxidation of carbon monoxide. *Mol. Catal.* **2017**, *442*, 173–180. [CrossRef]
56. Scirè, S.; Liotta, L.F. Supported gold catalysts for the total oxidation of volatile organic compounds. *Appl. Catal. B* **2012**, *125*, 222–246. [CrossRef]
57. Drits, V.A.; Eberl, D.D.; Srodon, J. XRD measurement of mean thickness, thickness distribution and strain for illite and illite-smectite crystallites by the Bertaut-Warren-Averbach technique. *Clays Clay Miner.* **1998**, *46*, 38–50. [CrossRef]
58. Gómez-Sainero, L.M.; Baker, R.T.; Vizcaíno, A.J.; Francis, S.F.; Calles, J.A.; Metcalfe, I.S.; Rodriguez, J.J. Steam Reforming of Methanol with Sm₂O₃-CeO₂-Supported Palladium Catalysts Influence of the Thermal Treatments of Catalyst and Support. *Ind. Eng. Chem. Res.* **2009**, *48*, 8364–8372. [CrossRef]
59. Ou, T.-C.; Chang, F.-W.; Roselin, L.S. Production of hydrogen via partial oxidation of methanol over bimetallic Au-Cu/TiO₂ catalysts. *J. Mol. Catal. A Chem.* **2008**, *293*, 8–16. [CrossRef]
60. Booi, E.; Klopogge, J.T.; Rob van Veen, J.A. Large pore REE/Al pillared bentonites: Preparation, structural aspects and catalytic properties. *Appl. Clay Sci.* **1996**, *11*, 155–162. [CrossRef]
61. Auprêtre, F.; Descorme, C.; Duprez, D. Bio-ethanol catalytic steam reforming over supported metal catalysts. *Catal. Commun.* **2002**, *3*, 263–267. [CrossRef]
62. Xi, H.; Hou, X.; Liu, Y.; Qing, S.; Gao, Z. Cu-Al spinel oxide as an efficient catalyst for methanol steam reforming. *Angew. Chem.* **2014**, *53*, 11886–11889. [CrossRef] [PubMed]
63. Liu, Y.; Qing, S.; Hou, X.; Qin, F.; Wang, X.; Gao, Z.; Xiang, H. Temperature dependence of Cu-Al spinel formation and its catalytic performance in methanol steam reforming. *Catal. Sci. Technol.* **2017**, *7*, 5069–5078. [CrossRef]

